Nucleic Acids Research, 2026, **54**, gkag553
https://doi.org/10.1093/nar/gkag553
Gene regulation, Chromatin and Epigenetics

RNAPII and DNA supercoiling regulate cohesin engagement in neurons

Morgan Crewe[1,2], Ilse Delint-Ramirez[1,2], Omar Halawa[1,3], Lance Heady[1,2], Ram Madabhushi[1,2,*]

[1]Departments of Psychiatry, Neuroscience, and Cell Biology, University of Texas Southwestern Medical Center, Dallas, TX 75390, United States
[2]Peter O'Donnell Brain Institute, University of Texas Southwestern Medical Center, Dallas, TX 75390, United States
[3]Lyda HIll Department of Bioinformatics, University of Texas Southwestern Medical Center, Dallas, TX 75390, United States

*To whom correspondence should be addressed. Email: ram.madabhushi@utsouthwestern.edu

Abstract

Chromatin looping by CTCF and cohesin is thought to be crucial for chromosome organization and gene transcription. Yet the precise relationships between CTCF, cohesin, and transcription in neurons are still poorly understood. To address this issue, we compared the occupancy of CTCF and the cohesin subunits, SMC1 and RAD21, relative to transcriptionally engaged RNAPII and as a function of stimulus-dependent transcription in cultured mouse cortical neurons. We show that CTCF and cohesin are enriched at transcription start sites (TSS) and that their levels increase with the level of transcriptionally engaged RNAPII, suggesting that RNAPII facilitates CTCF and cohesin occupancy. Unexpectedly, while neuronal stimulation caused widespread transcriptional activation, it resulted in the rapid genome-wide loss of SMC1 and RAD21 signals, including at the TSS of genes, loop anchors, and topologically associating domain boundaries. Activity-dependent reductions in cohesin were independent of CTCF but were mimicked by inhibiting either topoisomerase I or topoisomerase IIβ, which resolve torsional stress from DNA supercoiling. We show that neuronal stimulation elevates DNA supercoiling and that increasing torsional stress triggers the dissociation of cohesin from chromatin. Overall, these results suggest that modulation of torsional stress could be a physiologically relevant mechanism of regulating cohesin engagement and chromatin architecture.

Graphical abstract

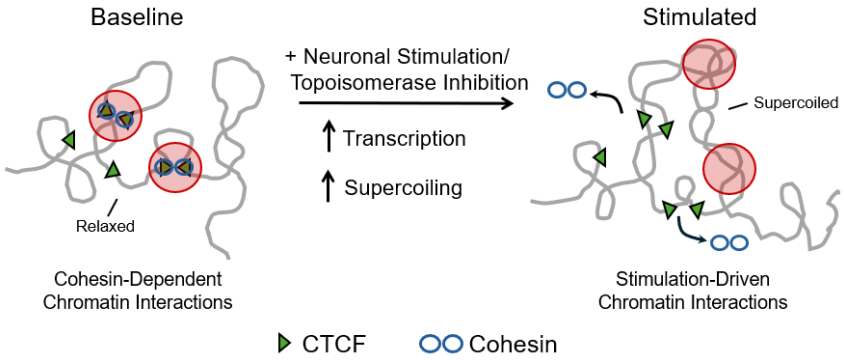

Introduction

Mammalian chromosomes are highly organized within the nucleus. At the basic level, DNA is wrapped around histone octamers in nucleosomes [1]. Beyond nucleosomes, chromosomes are folded into loops, and transcriptionally active and inactive regions segregate into distinct compartments [2–4]. Chromosome organization at each of these levels affects gene activity, and defects in chromosome architecture manifest in various developmental and progressive diseases [5–9]. This is especially the case for postmitotic neurons, where gene expression patterns are often established and modified over many years. Furthermore, exposure to new experiences alters chromosome structure and affects gene expression programs in neurons that are crucial for forming long-term memories and other adaptative behaviors [10–13]. Understanding the mechanisms that establish and modify chromatin structure in neurons is therefore significant.

In this regard, recent reports have focused on the roles of the cohesin complex in chromosome organization and gene regulation. Cohesin is a member of the structural maintenance of chromosomes (SMC) family of protein complexes. In mammalian cells, this complex is composed of a dimer of SMC1

Received: December 8, 2024. **Revised:** May 5, 2026. **Accepted:** May 17, 2026

and SMC3, the klesin RAD21, a stromal antigen protein subunit, either STAG1 or STAG2, and NIBPL and MAU2. The NIPBL-MAU2 heterodimer is essential for cohesin loading onto chromatin and for its ability to extrude DNA [14, 15]. Cohesin is unloaded from chromatin by the substitution of NIBPL-MAU2 with PDS5A/PDS5B and WAPL [14, 15]. Although initially studied for its role in mediating sister chromatid cohesion and their bi-orientation during mitosis, it was subsequently shown that cohesin also folds chromosomes into loops in interphase and postmitotic cells [16–18]. The mechanism of chromosome folding by cohesin is described by the loop extrusion hypothesis, which proposes that cohesin uses ATP hydrolysis to reel and extrude chromatin to generate loops [19–23]. Extrusion of chromatin is halted when cohesin encounters either the architectural protein, CTCF bound to convergently oriented CTCF motifs or other roadblocks, such as RNAPII and R-loops [18, 24–27].

The loop extrusion hypothesis can explain how distal chromatin segments are brought into proximity for gene regulation, recombination, and the formation of DNA damage foci. Yet the mechanisms that regulate cohesin loading-unloading cycles and loop extrusion are still poorly understood. In neurons, for instance, how cohesin dynamics relates to stimulus-dependent changes in chromatin architecture and enhancer-promoter loops remains unclear [10, 28, 29]. Recent reports suggest that in addition to CTCF, RNAPII itself anchors cohesin-extruded loops, and RNAPII pausing at promoter-proximal regions stabilizes enhancer-promoter contacts [25, 26]. These observations indicate a need for further exploring the relationships between cohesin, CTCF, and transcriptionally engaged RNAPII. Furthermore, single-molecule studies indicate that the ability of CTCF to block cohesin-mediated loop extrusion can vary according to the level of DNA tension [30]. However, whether DNA tension also affects cohesin activity in cells is unclear.

To address these issues, we compared the occupancy patterns of cohesin, CTCF, and transcriptionally engaged RNAPII in cultured mouse cortical neurons. We report that the occupancy of CTCF and cohesin at transcriptional start sites (TSSs) correlates with the levels of nascent transcription. Unexpectedly, neuronal stimulation significantly reduced CTCF signals at the TSS and caused a genome-wide loss in cohesin occupancy, revealing how neuronal activity could impact chromosome structure. In efforts to understand how neuronal stimulation reduces cohesin engagement, we observed that levels of DNA supercoiling become rapidly elevated following neuronal stimulation. Artificially increasing the levels of supercoiling by inhibiting cellular topoisomerases was sufficient to trigger the dissociation of cohesin from neuronal chromatin. Overall, our results indicate that modulating DNA torsional stress through supercoiling could be a physiological mechanism to regulate loop extrusion and gene transcription.

Materials and methods

Reagents and datasets

A complete list of all reagents used in this study is available in Supplementary Table S1. The purpose for each of these reagents is noted within Supplementary Table S1 and throughout the following methods sections where appropriate. Publicly available next-generation sequencing datasets, including those generated in this study are listed in Supplementary Table S2.

Biological resources

Primary cortical neurons from E16 Swiss-Webster mice (Charles River) were dissociated and plated at a density of 500 000 cells/ml. Tissue-culture plates were pre-coated with 0.05 mg/ml poly-D-lysine at 37°C overnight, then washed twice with ddH_20 prior to plating. Cortical neurons were maintained in neurobasal media (GIBCO) supplemented with L-glutamine, penicillin/streptomycin, and B27. All drug treatments were added directly to the cell culture media, and a complete list of their usage can be found in Supplementary Table S1.

CTCF, SMC1, and RAD21 ChIP-seq

CTCF, SMC1, and RAD21 ChIP-seq experiments were performed as described previously [31]. Briefly, DIV13 primary cortical neurons (~1.5M cells per replicate) were crosslinked, lysed, and sonicated prior to immunoprecipitation using anti-CTCF (1:200, CST, #3418), anti-SMC1 (1:1000, Bethyl, A300-055A), or anti-RAD21 (1:1000, GeneTex, GTX106012) antibodies. Immunoprecipitated protein–DNA complexes were eluted and subjected to crosslink reversal and protein digestion. The resulting DNA samples were resuspended in TE buffer and prepared for sequencing using a paired-end library preparation kit (Roche) according to the manufacturer's instructions. Samples were pooled and sequenced on an Illumina NextSeq 500 instrument with V2.5 reagents to an average depth of 45–50 million reads per replicate.

ChIP-seq data analysis

All ChIP-seq data generated for this manuscript, as well as data generated in previously published work, were processed in accordance with ENCODE ChIP-seq analysis guidelines [32]. Trimmed FASTQ sequencing reads were aligned to the appropriate reference genome (mm10/GRCm38.p6 or hg38/GRCh38.p14) using *BWA-MEM*. Aligned BAM files were marked and filtered for duplicate reads using *samtools*. Peaks were called using *MACS2* [33] from biological duplicates and pseudo-replicates where each ChIP sample was normalized to input. For analysis of signal intensity, *MACS2*-generated bedGraph files were converted to bigWig files using kentUtils [34] for individual replicates and pooled replicates.

RNA-seq

Total RNA was extracted from three biological replicates of untreated and N-methyl-D-aspartate (NMDA)-treated DIV13 primary cortical neurons (~5 million cells per replicate) using the Qiagen RNeasy Plus Universal Kit (Qiagen). Samples were treated with DNase to remove any residual DNA. RNA concentration was measured by fluorometry (RNA high-sensitivity Qubit assay, Thermo), and RNA quality was assessed using an Agilent Tapestation 4200. Samples with a RIN score of 8 or higher were used for library preparation using a single-end library preparation kit (Illumina) according to the manufacturer's instructions. Samples were pooled and sequenced on an Illumina NextSeq 500 instrument with

V2.5 reagents to an average depth of 35–45 million reads per replicate.

RNA-seq data analysis

Raw FASTQ sequencing reads generated for this manuscript, as well as raw FASTQ data generated in previously published work, were analyzed for quality control using *FastQC*, trimmed using *Trimmomatic*, and aligned to appropriate reference genome (mm10/GRCm38.p6 or hg38/ GRCh38.p14) using *TopHat* [35]. Aligned reads were processed by the *HTSeq-Count* pipeline [36], and the resulting raw counts were used to calculate transcripts per million mapped fragments (TPM). Where indicated, raw counts were also used to identify significantly upregulated ($P < .05$, log fold-change > 1.2) or downregulated ($P < .05$, log fold-change < -0.5) transcripts using *deSeq2* [37].

Chromatin state and Gene Ontology analysis

ChromHMM [38] was used to segment the mm10 mouse genome into 15 chromatin states based on ENCODE data from mouse P0 forebrain for the eight indicated histone modifications. *ChromHMM OverlapEnrichment* was used to plot enrichment of the eight indicated histone modifications within the resulting 15-state model. SMC1, CTCF, and RAD21 ChIP-seq signal intensity was quantified within each of the 15 chromatin states using kentUtils *bigWigAverageOverBed* [34]. IDR-thresholded peaks from RAD21 ChIP-seq were annotated using ChIPseeker *annotatePeak* using the UCSC mm10 genome annotation database and default parameters [39]. Gene Ontology for known genes was analyzed via clusterProfiler *enrichGO* with default parameters and plotted [40].

Hi-C analysis

Previously published Hi-C data from iPSC-derived mouse cortical neurons [41] and hippocampal neurons from mice injected with the glutamate receptor agonist, kainic acid (KA) [42], were used to identify chromosome compartments, topologically associating domains (TADs), and chromatin loops using the Juicer suite [43]. Chromosome compartments were called using the Eigenvector command with a 500-kb resolution and KR normalization. TADs and chromatin loops were called using the Juicer Arrowhead and HiCCUPS algorithms, respectively, at 5-, 10-, and 25-kb resolutions with KR normalization. To enable fair cross-condition comparison of loop strength, loop calls across all three conditions (saline, KA 1 h, KA 48 h) from the 25-kb significant loops were merged into a unified set by clustering anchors to the nearest bin of the same size using a proximity-based DBSCAN approach, with the same defaults as hictoolsr's mergeBedpe implementation ($\epsilon = 50$ kb for 25 kb resolution), but retaining loops called as significant in at least one condition. This yielded 3307 total loops. Aggregate peak analysis (APA) was performed using Juicer Tools at 25-kb resolution with KR normalization (window = 10 bins, minimum distance = 30 bins), applying the merged union set to ensure fairness in anchor assignment across conditions. Loop strength was quantified using the peak-to-mean ratio (P2M) and peak-to-lower-left ratio (P2LL; corner width $q = 6$ bins), as well as the raw central pixel intensity. Hi-C data derived from hippocampal neurons were visualized with Juicebox [44] at 25-kb resolution and balanced normalization. Log (Expected/Observed) for each condition (saline and KA) as well as log (KA/saline) contact signals were plotted for the indicated chromosomal regions.

TMP incorporation assay

DIV13 primary cortical neurons (~10 M cells per replicate) plated in 10-cm tissue culture dishes were incubated with trimethylpsoralen (TMP, 12 μg/ml final) for 10 min at 37°C. Tissue culture dishes were then placed on ice and exposed to 3.6 kJ m^{-2} of 365-nm UV light (Spectronics, XL-1500UV) to achieve DNA:TMP crosslinking. Following UV crosslinking, neurons were immediately collected in 1ml sodium dodecyl sulfate (SDS) lysis buffer [50 mM Tris–HCl, pH 8.1, 10 mM ethylenediaminetetraacetic acid (EDTA), 1% SDS] and incubated with 100 μg/ml Proteinase K (NEB) overnight at 55°C. Genomic DNA was extracted using phenol/chloroform, precipitated with ethanol, resuspended in 200 μl ddH_2O plus RNase A (1 μg Invitrogen), and incubated for 2 h at 37°C. Genomic DNA was again isolated using phenol/chloroform, precipitated with ethanol, and diluted to a concentration of 0.12 mg/ml in elution buffer (EB; 10 mM Tris–HCl, pH 8.0). DNA samples were then sonicated manually (5 × 30 s, Cole Palmer ultrasonic processor) then further sonicated in a Bioruptor Plus (high, 40 cycles, 30 s on/off) to achieve fragment sizes of 250–350 bp. To enrich crosslinked DNA fragments, samples were subjected to three rounds of ExoI digestion. Samples were boiled for 10 min at 95°C, cooled on ice for 2 min, and incubated with ExoI buffer (10 μl of 10× buffer, NEB) and ExoI enzyme (10 μl, NEB) for 1 h at 37°C. Additionally, a fraction of each sample was removed prior to ExoI digestion as a total DNA loading control. Following ExoI digestion, clean DNA was extracted using a polymerase chain reaction clean-up kit (QIAquick, Qiagen), and samples were quantified using fluorometry (double-stranded DNA high sensitivity Qubit assay, Thermo). To assess total levels of TMP crosslinking, samples were electrophoresed on a 1% agarose gel, post-stained with GelRed (Biotium), and imaged on a Bio-Rad Chemidoc system. Samples that were not exposed to UV crosslinking (uncrosslinked, UNX) and samples that were not subjected to ExoI digestion were used to control for the level of ExoI digestion achieved and for DNA loading controls, repsectively.

TMP levels are represented as signal intensity normalized by the intensity of total DNA that was not subjected to ExoI digestion.

Chromatin fractionation and western blotting

DIV13 primary cortical neurons (~5 M cells per replicate) were washed three times with cold phosphate-buffered saline and lysed in 500 μl lysis buffer (20 mM HEPES, 2 mM $MgCl_2$, 10 mM KCl, 1 mM EDTA, 1 mM Elthylene Glycol Tetraacetic acid (EGTA), 1 mM Dithiothreitol (DTT), and 0.5 × protease and phosphatase inhibitors; pH 7.4) for 15–20 min on ice. Lysates were sheared through a 25-gauge needle and centrifuged at 750 × *g* for 5 min at 4°C to separate the cytosolic fraction (supernatant). The pellet was resuspended in 500 μl lysis buffer, centrifuged at 750 × *g* for 5 min, and the supernatant was discarded. The pellet was resuspended in 200 μl CSK-D buffer (10 mM PIPES, 100 mM NaCl, 300 mM sucrose, 1 mM EGTA, 1 mM $MgCl_2$, 1 mM DTT, 0.5% Triton X-100, and protease and phosphatases inhibitors), incubated for 10 min on ice, and centrifuged at 6800 × *g* for 3 min at 4°C to separate the nuclear fraction (supernatant). The pellet was

resuspended in 100 µl benzonase buffer (10 mM Tris–HCl, pH 8, 2 mM $MgCl_2$, 0.5% Triton X-100) and centrifuged at 6800 × *g* for 3 min. The supernatant was discarded, and the pellet was resuspended in 100 µl benzonase buffer plus benzonase enzyme (1:50, Sigma, E1014). Samples were incubated overnight at 4°C with gentle agitation. The following day, samples were vortexed briefly and incubated for an additional 30 min at room temperature. A final centrifugation at 1000 × *g* for 5 min at 4°C yielded the chromatin fraction (supernatant) and the nuclear matrix fraction (pellet). The nuclear matrix fraction was resuspended in 100 µl CSK-D buffer. Final protein concentration in each fraction was measured via BCA assay (Thermo). Western blotting for SMC1, SMC3, RAD21, CTCF, RNAPII, Actin, and H2AX was carried out via standard western blotting procedures (see Supplementary Table S1 for antibody details). Signal intensity for the protein of interest was quantified using ImageJ, normalized to loading controls, and expressed as fold change over untreated controls. Graphs were generated using GraphPad Prism 9.

Visualization and statistical analysis

All aggregate plots were generated from score matrices using deepTools *computeMatrix* [45]. Where a single centered region is denoted on the *x*-axis, aggregate plots were generated in reference-point mode [center = peak summit (SMC1/CTCF/RAD21), signal averaged over 50 bp bins, upstream and downstream flanking distance noted on *x*-axis]. Where both the TSS and TES of transcripts of interest are denoted on the *x*-axis, aggregate plots were generated in scale-regions mode (TSS to TES scaled to 1 kb, signal averaged over 50-bp bins, upstream and downstream flanking distances noted on *x*-axis). Scale-regions mode was also utilized to generate aggregate plots of SMC1 or CTCF signal within/surrounding TADs and chromatin loops (END to END scaled to 5 kb, signal averaged over 50-bp bins, upstream and downstream flanking distances noted on *x*-axis), as well as chromosome compartments (END to END scaled to 10 kb, signal averaged over 50-bp bins, no flanking distance shown). Matrices from *computeMatrix* outputs were plotted using *plotprofile*. Signal intensity within 1 kb surrounding the TSS was quantified using kentUtils *bigWigAverageOverBed* [34]. Differences in median signal intensity were analyzed for significance via Wilcoxon signed-rank, Mann–Whitney U or Kruskal–Wallis analysis of variance (ANOVA), and median signal intensity ± 95% confidence intervals were graphed using GraphPad Prism 9. Screenshots of signal tracks were generated using UCSC Genome Browser.

Results

SMC1 and CTCF occupancy on chromatin correlates with RNAPII activity in neurons

We performed ChIP-seq to examine the occupancy patterns of CTCF and the cohesin subunit, SMC1 [31]. Separately, we performed RNA-seq and mapped the sites of transcriptionally engaged RNAPII in untreated mouse cortical neurons by performing GRO-seq (fastGRO) [46]. Here, we analyzed these datasets to decipher the relationships between CTCF, SMC1, and engaged RNAPII.

As a first step, RNA-seq data from untreated neurons was used to classify genes as either expressed (TPM > 1) or silent (TPM < 1), and the distribution of CTCF and SMC1 was analyzed relative to these groups. CTCF and SMC1 signals were elevated at the TSS of both expressed and silent genes; however, expressed genes accumulated higher levels of both proteins at their TSS compared to silent genes, indicating that transcription could affect CTCF and SMC1 occupancy (Fig. 1A–C). To further explore this possibility, we analyzed our fastGRO data obtained from cultured mouse cortical neurons using two different schemes: (i) fastGRO FPKMs (fragments per kilobase million) in known and annotated genes were used to rank and group genes into quartiles of expression (Q1 – low, Q4 – high; Supplementary Fig. S1A); (ii) transcript/gene annotations based on the reference mouse genome were ignored, and the *de novo* transcript identification tool in HOMER was instead used to independently call transcripts based on fastGRO signal accumulation patterns alone [47]. This analysis yielded 25 253 *de novo* transcripts in cultured cortical neurons, and fastGRO FPKMs were again used to group *de novo* transcripts into expression quartiles (Q1 – low, Q4 – high; Supplementary Fig. S1B). *De novo* transcripts are called by scanning the genome for stereotypical patterns of transcriptionally engaged RNAPII and represent RNAPII activity at a variety of sites besides known genes, including enhancers and other noncoding RNAs [47, 48]. We reasoned that this approach would allow us to identify sites of elevated RNAPII activity independent of gene annotation and assess how CTCF and SMC1 bind relative to such sites in an unbiased manner. The levels of CTCF and SMC1 signals at the TSS of *de novo* transcripts increased with increasing levels of transcription (Fig. 1D and E). The levels of CTCF and SMC1 were also elevated at the TSS of Q4–Q2 known genes compared to Q1 known genes, although differences between Q4 and Q2 known genes were less apparent (Supplementary Fig. S1C and D). Recent reports suggest that RNAPII could anchor cohesin-extruded loops, thereby stimulating its accrual at the TSS of expressed genes [25, 26]. Consistent with this scenario, SMC1 signals at the TSS were bookended by CTCF upstream and transcriptionally engaged RNAPII downstream in annotated genes and *de novo* transcripts (Fig. 1C and F–H; Supplementary Fig. S1E). Overall, these results indicate that the enrichment of CTCF and SMC1 at the TSS correlates with levels of transcriptionally engaged RNAPII in neurons.

Neuronal activity triggers the disengagement of cohesin

Neuronal activation triggers the transcription of hundreds of genes and the engagement of RNAPII at thousands of putative enhancers. To determine how this increase in transcriptionally engaged RNAPII affects the occupancy of CTCF and SMC1, we stimulated cultured mouse cortical neurons with the glutamate receptor agonist, NMDA (50 µM for 10 min followed by washout and recovery for 50 min). NMDA stimulation recapitulates the patterns of synapse-to-nucleus communication and stimulus-dependent gene expression that have been observed in relevant brain areas following exposure of animals to physiological learning behaviors. RNA-seq data from NMDA-treated neurons were ranked and grouped into expression quartiles as described earlier (Q1 – low; Q4 – high). The distribution of CTCF and SMC1 signals were then analyzed at these groups of genes. As in untreated neurons, CTCF and SMC1 signals were elevated at Q4–Q2 genes compared to Q1 genes in NMDA-treated neurons, indicating again that the occupancy of both proteins at the TSS correlate with the

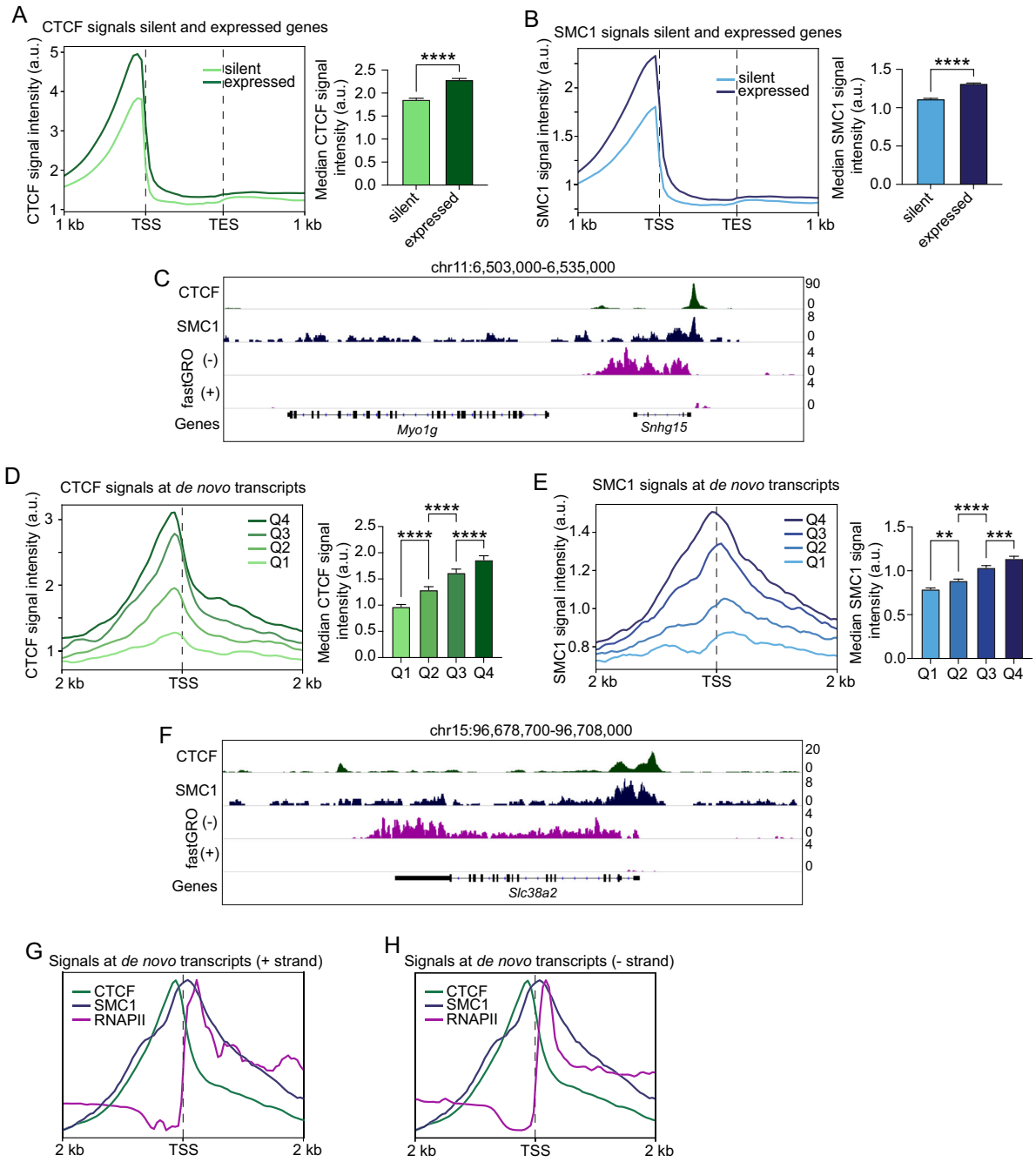

Figure 1. CTCF and SMC1 occupancy correlates with transcriptionally engaged RNAPII. (**A**, **B**) We performed CTCF and SMC1 ChIP-seq and RNA-seq in untreated DIV13 mouse primary cortical neurons to assess the relationship between CTCF, SMC1, and gene transcription. RNA-seq data were used to classify silent (TPM < 1) or expressed (TPM > 1) genes. Average CTCF (A) or SMC1 (B) signal intensity surrounding silent and expressed genes (left) with quantification of median signal intensity (right, Mann–Whitney U, $P < .0001$) are shown. (**C**) Representative genome browser view of CTCF ChIP-seq, SMC1 ChIP-seq, and fastGRO signals at silent (*Myo1g*) and expressed (*Sngh15*) mouse genes in untreated primary cortical neurons. fastGRO signals are shown for both the minus (–) and plus (+) DNA strands. Range of signal intensity for each track is shown on the right axis. (**D**, **E**) We utilized our previously published fastGRO data obtained from untreated mouse primary cortical neurons to more precisely clarify how CTCF and SMC1 occupancy correlate with RNAPII activity. The *de novo* transcript identification tool in HOMER was used to identify transcripts based on RNAPII occupancy/fastGRO signal accumulation patterns rather than strictly adhering to known transcript/gene annotations. Next, fastGRO FPKMs were used to rank *de novo* transcripts into expression quartiles (Q1 – low, Q4 – high) to assess the relationship between fastGRO signal and CTCF/SMC1 occupancy. Average CTCF (D) and SMC1 (E) signal intensity surrounding *de novo* transcript quartiles (left) and quantification of median signal intensity (right, Kruskal–Wallis ANOVA, $**P < .01$, $***P < .001$, $****P < .0001$) are shown. (**F**) Representative genome browser view of CTCF ChIP-seq, SMC1 ChIP-seq, and fastGRO signals at an expressed mouse gene (*Slc38a2*) in untreated primary cortical neurons. fastGRO signals are shown for both the minus (–) and plus (+) DNA strands. Range of signal intensity for each track is shown on the right axis. (**G**, **H**) fastGRO signals were used as a proxy for RNAPII occupancy to further investigate the relationship between CTCF, SMC1, and RNAPII binding patterns. Due to inherent differences in maximum signal intensity between experiments, aggregate plots of average signal intensity surrounding *de novo* transcripts were independently generated for CTCF ChIP-seq, SMC1-seq, and fastGRO. Individual plots were then merged to create a single aggregate plot depicting CTCF, SMC1, and RNAPII binding patterns relative to one another, irrespective of signal intensity. Merged aggregate signals are shown surrounding fastGRO *de novo* transcripts on both the plus (G) and minus (H) DNA strands.

level of transcription (Supplementary Fig. S2A and B). Unexpectedly, however, overall levels of CTCF and SMC1 at the TSS were reduced in NMDA-treated neurons compared to their levels in untreated neurons (Fig. 2A–E and Supplementary Fig. S2C). Next, RNA-seq data from untreated and NMDA-treated neurons were compared to identify either upregulated or downregulated genes following neuronal stimulation. CTCF and SMC1 signals were then analyzed at these genes. CTCF and SMC1 were reduced at the TSS of both upregulated and downregulated genes in NMDA-treated neurons compared to their respective levels at these sites in untreated neurons (Fig. 2F–I). These results suggest that neuronal stimulation causes the disengagement of CTCF and cohesin from the TSS regardless of the level of transcriptionally engaged RNAPII.

To understand whether reductions in CTCF and SMC1 following neuronal stimulation was restricted to the TSS or whether they also occurred at other sites, neuronal chromatin was classified into 15 distinct states (various classes of promoters, enhancers, transcribed regions, and heterochromatin) based on the occupancy patterns of eight key histone marks (Supplementary Fig. S2D) [38, 49, 50]. CTCF and SMC1 levels in each chromatin state were then measured as a function of neuronal stimulation. CTCF signals were reduced at promoters in NMDA-treated neurons compared to controls but not in other states (Fig. 3A). By contrast, decreased SMC1 signals were observed at 14/15 states (H3K9me3-rich heterochromatin being the exception) in NMDA-treated neurons compared to controls (Fig. 3B). These results suggest that neuronal stimulation causes widespread losses in cohesin occupancy while reductions in CTCF are limited to promoters.

To determine how the loss of cohesin across most chromatin states relates to higher-order chromosome organization, Hi-C data from cultured mouse cortical neurons were used to identify loops, TADs, and chromosome compartments. CTCF and SMC1 patterns were then analyzed relative to these features [41]. As expected, CTCF and SMC1 signals were enriched at loop and TAD boundaries (Fig. 3C–F). SMC1 levels, but not CTCF levels, were reduced across loops and TADs, including at their boundaries, in NMDA-treated neurons compared to untreated controls (Fig. 3C–F). CTCF signals across chromosome compartments were also unaffected by NMDA treatment (Fig. 3G). By contrast, SMC1 levels decreased across chromosome compartments, particularly in transcriptionally active compartments A in NMDA-treated neurons (Fig. 3H). These results together indicate that neuronal stimulation specifically causes the disengagement of cohesin genome-wide.

Cohesin organizes mammalian chromosomes into loops and TADs, and cohesin loss results in widespread elimination of looping contacts [14, 18]. Cohesin disengagement following neuronal stimulation could therefore manifest in reduced chromosome contact frequencies. To test whether existing data support such a possibility, we reanalyzed publicly available Hi-C data from hippocampal neurons of mice that were injected with either the glutamate receptor agonist, KA, or with saline controls [42]. Whereas overall compartmental and TAD patterns were similar across conditions, visual inspection of observed/expected contact maps suggested that contact frequencies and loop domains were reduced across chromosomes 1 h post-KA treatment compared to saline controls (Supplementary Fig. S3 and Fig. 4A). These trends became further apparent when contact maps from neurons isolated 1 h post-KA were normalized to those from saline-treated samples (Supplementary Fig. S3 and Fig. 4B). Similarly, the number of intrachromosomal loops and TADs was reduced by 1 h post-KA treatment compared to saline controls (Fig. 4C and D). Aggregate peak analysis (APA) revealed that loop strength, as indicated by lower raw pixel intensities and lower Peak to Mean (P2M) scores, also decreased by 1 h post-KA treatment (Fig. 4E).

Analysis of Hi-C data generated from neurons 48 h post-KA treatments suggested that activity-dependent reductions in chromosomal contacts and loop numbers were transient. In fact, normalized contact frequencies, the numbers of loops and TADs, and loop strength were all elevated 48 h post-KA exposure compared to saline controls (Supplementary Figs S3 and S4A–E). Overall, the reduction in intrachromosomal contacts following KA exposure is in line with our observations of an activity-dependent decrease in cohesin occupancy in cultured neurons.

TOP2B inhibition is sufficient to induce cohesin disengagement from chromatin in neurons

Single-molecule experiments indicate that the effects of CTCF on loop-extruding cohesin can vary depending on the level of DNA tension [30]. However, the impact of DNA mechanical stress on cohesin activity in cells is unclear. Dynamic supercoiling generated from transcription is a major source of DNA torsional stress in eukaryotic cells, with DNA unwinding by RNAPII generating twin domains of overwound DNA ahead, and underwound DNA behind RNAPII (Supplementary Fig. S4A) [51–57]. These observations prompted us to investigate whether altered supercoiling in response to neuronal stimulation could underlie changes in cohesin occupancy.

To assess how neuronal activity affects DNA supercoiling, we utilized 4,5′,8-trimethylpsoralen (TMP) to preferentially crosslink underwound DNA in neurons [57]. Untreated and NMDA-treated cultured mouse cortical neurons were incubated with TMP and irradiated with 360-nm light to induce crosslinking. Genomic DNA isolated from TMP-treated and UV-crosslinked neurons was fragmented by sonication and subjected to three rounds of heat denaturation and Exo I digestion (Supplementary Fig. S4B). Omission of TMP resulted in almost complete digestion of genomic DNA by Exo I (Unx), while TMP-treated samples were resistant, indicating successful crosslinking in these experiments (Fig. 5A). Genomic DNA isolated from NMDA-treated neurons was significantly more resistant to Exo I digestion compared to untreated neurons (Fig. 5A), suggesting that neuronal stimulation causes increased DNA tension from supercoiling.

DNA supercoiling is resolved by cellular topoisomerases, and inhibiting topoisomerases elevates DNA supercoiling [52, 55, 56]. Consistent with this idea, treatment of cultured cortical neurons with either the TOP1 inhibitor camptothecin (CPT) or the TOP2 inhibitor, etoposide (ETP) elevated bulk TMP crosslinking compared to untreated controls, indicated increased DNA supercoiling (Supplementary Fig. S4C). Whereas neurons express both TOP1 and TOP2B, we previously reported that neuronal activity modulates TOP2B activity and that elevated supercoiling following TOP2B inhibition affects neuronal transcription [46, 58–60]. To test how elevated supercoiling affects CTCF and cohesin occupancy, we therefore incubated cultured mouse cortical neurons with ETP (10 μM for 1 h) and performed CTCF and SMC1 ChIP-seq.

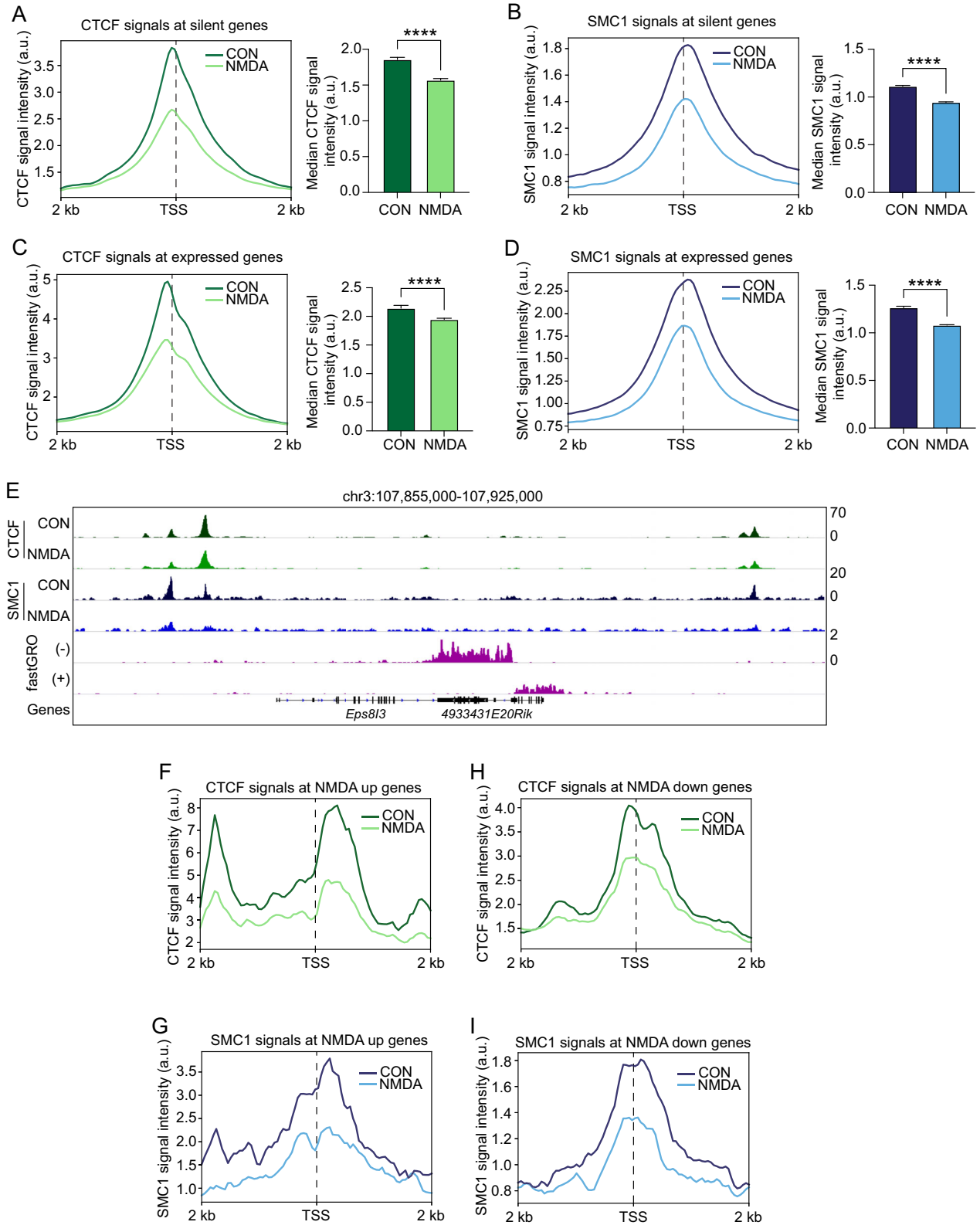

Figure 2. Neuronal activity triggers the disengagement of SMC1 and CTCF. (**A**, **B**) CTCF and SMC1 ChIP-seq signals were assessed in cultured primary cortical neurons stimulated with N-methyl-D-aspartic acid (NMDA; 50 μM, 10 min). Aggregate plot (left) and quantification (right) of average CTCF (A) and SMC1 (B) signals in control and NMDA-treated neurons at silent genes defined as in Fig. 1A are shown (Mann–Whitney U, $P < .0001$). Aggregate plot (left) and quantification (right) of average CTCF (**C**) and SMC1 (**D**) signals in control and NMDA-treated neurons at expressed genes defined as in Fig. 1A (Mann–Whitney U, $P < .0001$). (**E**) Representative genome browser views depicting CTCF and SMC1 signals in control and NMDA-treated neurons as well as fastGRO signal on both the minus (−) and plus (+) DNA strands in control neurons. (**F**, **G**) RNA-seq was performed in untreated and NMDA-treated (50 μM, 10 min) cultured primary cortical neurons. DeSeq2 was used to identify significantly upregulated ($n = 86$) and downregulated ($n = 892$) genes following NMDA treatment. Aggregate plots of average CTCF (F) and SMC1 (G) signals in control and NMDA-treated neurons at genes that are upregulated following NMDA treatment are shown. Aggregate plots of average CTCF (**H**) and SMC1 (**I**) signals in control and NMDA-treated neurons at genes that are downregulated following NMDA treatment.

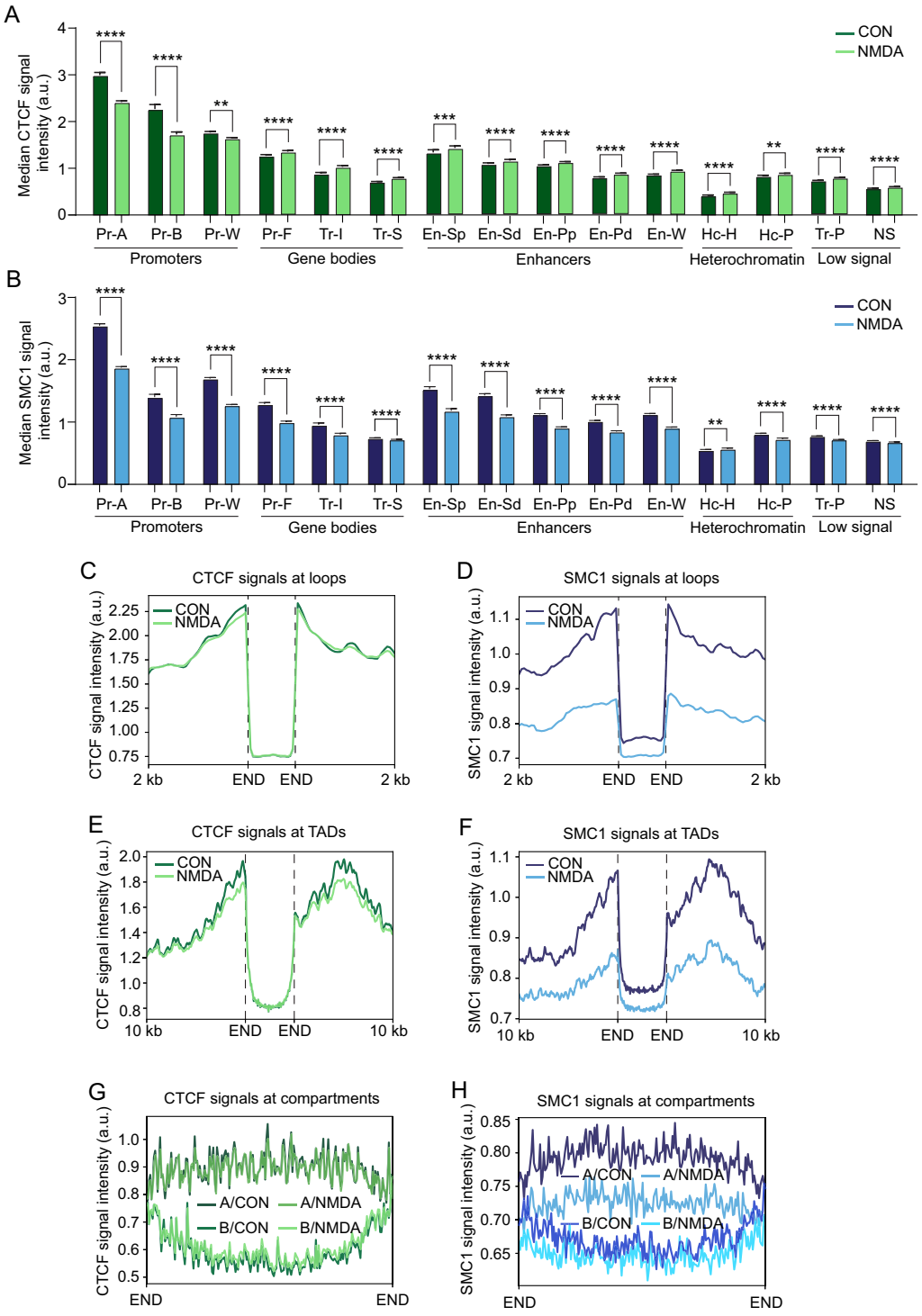

Figure 3. Global loss of SMC1 but not CTCF following neuronal stimulation. (**A**) Fifteen distinct chromatin states across the mouse genome were categorized using ChIP-seq signals for eight histone modifications in P0 mouse forebrain via ChromHMM. The distribution of CTCF ChIP-seq signal intensity in untreated and NMDA-treated neurons is shown for promoters (active promoters, Pr-A; bivalent promoters, Pr-B; and weak promoters, Pr-W), gene bodies (promoter flanking, Pr-F; transcriptional initiation, Tr-I; strong transcription, Tr-S), enhancers (strong proximal enhancers, En-Sp; strong distal enhancers, En-Sd; poised proximal enhancers, En-Pp; poised distal enhancers, En-Pd), heterochromatin (H3K36me3-rich heterochromatin, Hc-H; polycomb repressive heterochromatin, Hc-P), and regions that have low or no signal for any of the chromatin modifications surveyed (transcriptionally permissive/open regions, Tr-P; no signal, NS). Quantifications are shown for median CTCF signal in control versus NMDA-treated neurons (Wicoxon signed-rank test, $**P < .01$, $***P < .001$, $****P < .0001$). For full description of ChromHMM states, see Supplementary Fig. S2D. (**B**) Distribution of SMC1 ChIP-seq signal intensity in untreated and NMDA-treated neurons across chromatin states as described in panel (A). (**C**, **D**) Previously published Hi-C data from cortical neurons was used to assess stimulation-dependent changes in CTCF and SMC1 signal intensity at chromatin loops and TADs. Aggregate plots of average CTCF (C) and SMC1 (D) signals within/surrounding chromatin loops in control and NMDA-treated neurons are shown. Aggregate plots of average CTCF (**E**) and SMC1 (**F**) signals within/surrounding TADs in control and NMDA-treated neurons. (**G**, **H**) Previously published Hi-C data were also used to segregate the genome into A and B chromosome compartments. Aggregate plots of average CTCF (G) and SMC1 (H) signals within compartments A and B in control and NMDA-treated neurons are shown.

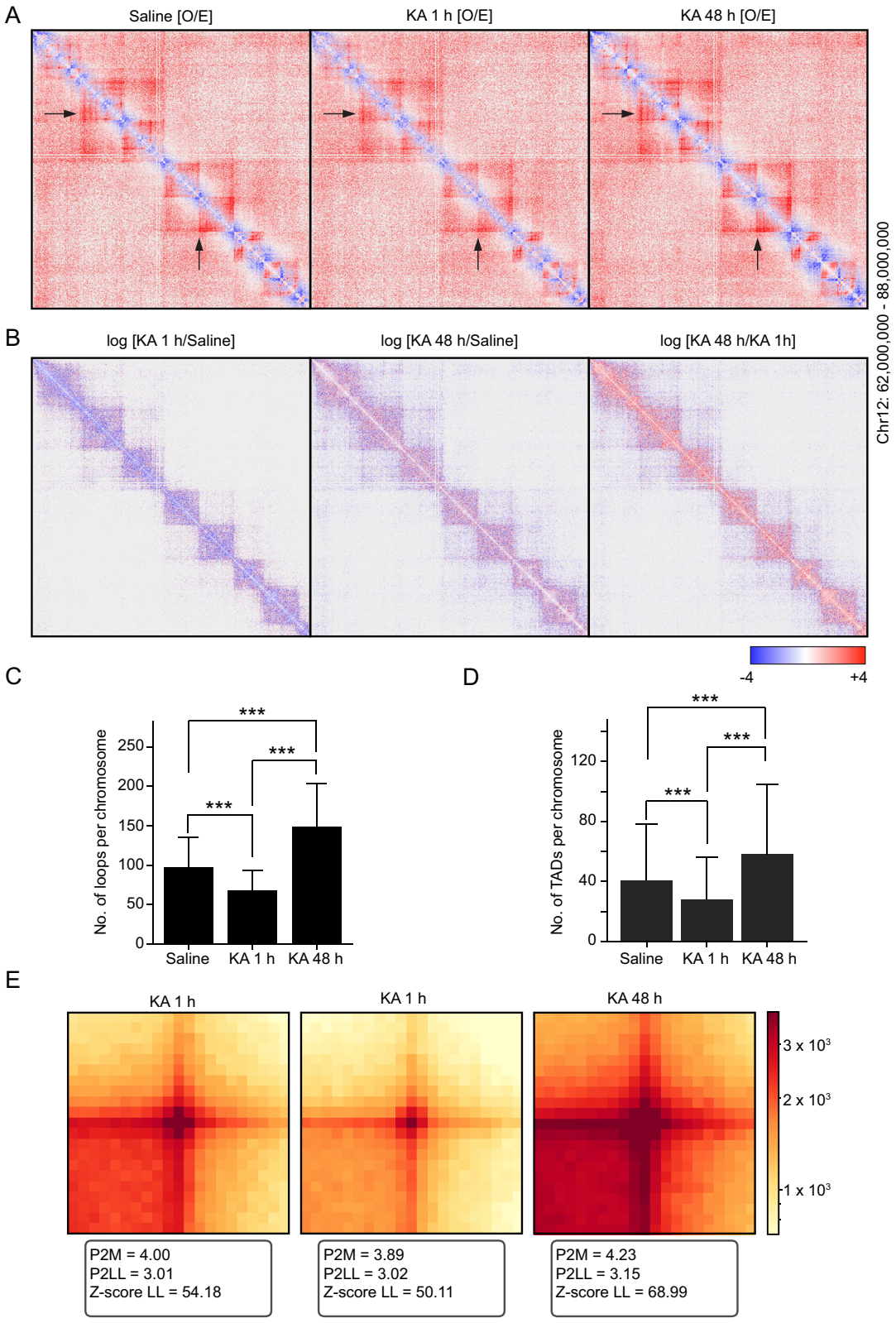

Figure 4. Chromosome contacts and loops are transiently reduced following neuronal activity *in vivo*. (**A**) Hi-C data from hippocampal neurons of mice that were either treated with saline controls or a single dose of KA followed by recovery for either 1 or 48 h [42] were re-analyzed. Log (observed/expected) contact maps from a representative region on mouse chromosome 12 at 25-kb resolution and with KR (balanced) normalization are shown across the three conditions. Arrows indicate regions with reduced contacts at 1 h post-KA but relatively increased contacts at 48 h post-KA compared to saline. (**B**) Saline-control-normalized contact maps of KA-treated neurons at the same interval and resolution as in panel (A) (left and middle panels). Additionally, contact maps from KA-treated neurons after 48-h recovery were normalized to those after 1-h recovery (right). Scale indicates the direction of observed and relative contact frequencies in both panels (A) and (B). Number of loops (**C**) and TADs (**D**) across 5, 10, and 25 kb resolutions were compared across the three conditions (***$P < .0001$, Wilcoxon test for both Saline v KA 1 h and Saline v KA 48 h for both loops and TADs per chromosome). (**E**) APA plot showing the aggregate signal from 3300 loops. The scale on the right indicates pixel intensity. Loop strength as indicated by Peak to Mean score and Peak to Lower Left (P2LL) and its associated Z-score (Z-score LL) are shown.

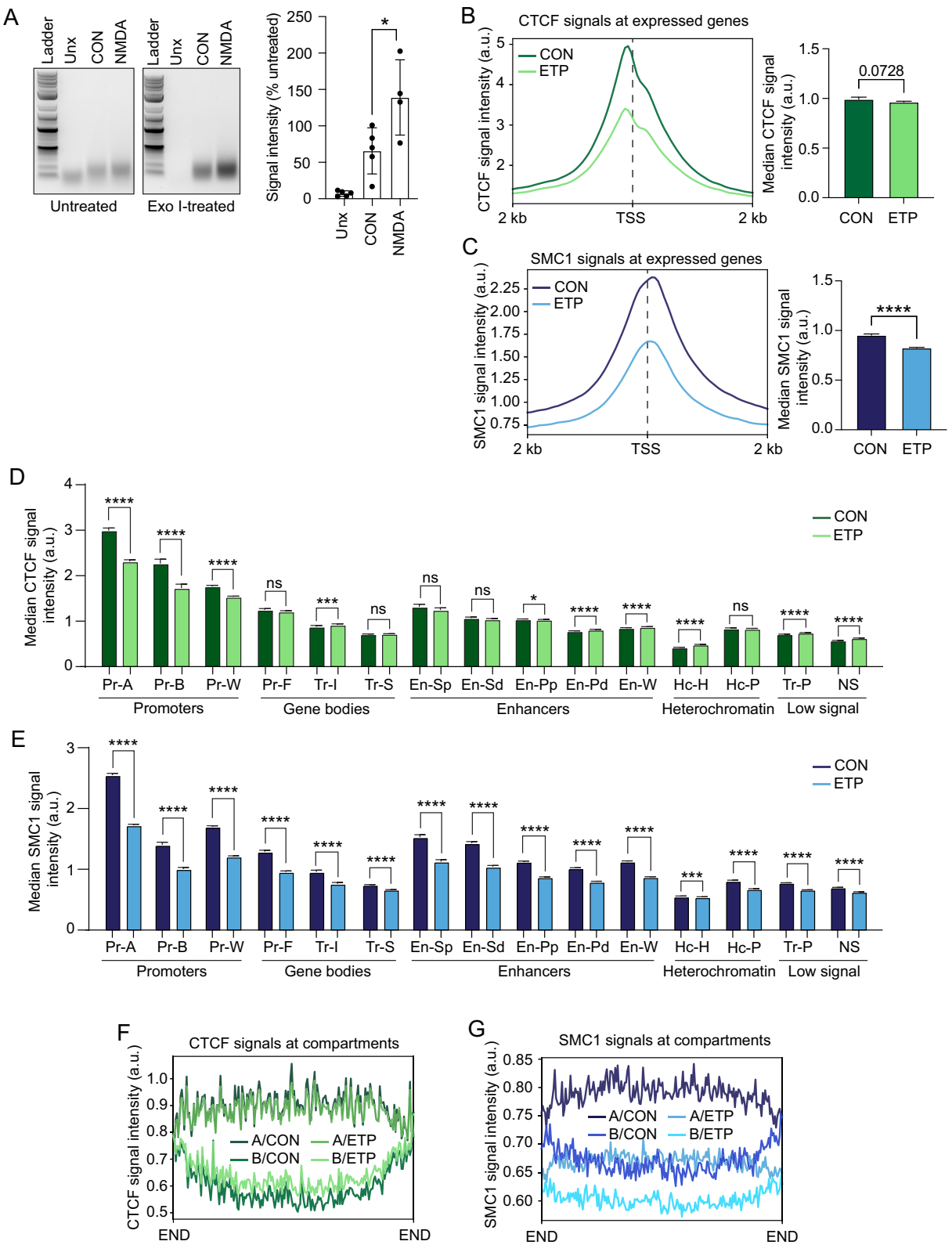

Figure 5. TOP2B inhibition is sufficient to induce cohesin disengagement from chromatin in neurons. (**A**) Trimethylpsoralen (TMP) incorporation and crosslinking was used to assess the levels of negative DNA supercoiling in control and NMDA-treated cultured primary cortical neurons. Exo I was used to digest all DNA without negative supercoiling/TMP incorporation, and untreated (without Exo I) samples were used as a loading control. Quantification of normalized signal intensity in Exo I-treated samples is also shown (right, one-way ANOVA, $P < .01$). For a diagram of the TMP incorporation protocol, see Supplementary Fig. S2B. Unx - uncrosslinked with TMP (**B**, **C**) To assess the role of DNA supercoiling in SMC1 dissociation, cultured primary cortical neurons were treated with the TOP2 poison etoposide (ETP, 10 μM, 1 h). Aggregate plot (left) and quantification (right) of average CTCF (C) and SMC1 (D) signals in control and ETP-treated neurons at expressed genes defined as in Fig. 1A (Mann–Whitney U, $P < .0001$). Distribution of CTCF (**D**) and SMC1 (**E**) ChIP-seq signal intensity in untreated and ETP-treated neurons across chromatin states as described in Fig. 3A (Wilcoxon signed-rank test, $*P < .05$, $**P < .01$, $***P < .001$, $****P < .0001$). Aggregate plots of average CTCF (**F**) and SMC1 (**G**) signals within compartments A and B in control and ETP-treated neurons.

Similar to NMDA-treated neurons, CTCF and SMC1 levels were reduced at the TSS in ETP-treated neurons compared to untreated controls (Fig. 5B and C; Supplementary Fig. S4D and E). In fact, ETP-treated neurons mimicked the activity-dependent loss of SMC1, but not CTCF, at most chromatin states (Fig. 5D and E), loop anchors (Supplementary Fig. S4F and G), TAD boundaries (Supplementary Fig. S4H and I), and chromosome compartments (Fig. 5F and G).

To further verify that changes in SMC1 occupancy following neuronal stimulation and TOP2B inhibition reflect changes in cohesin binding, we assessed the occupancy of a distinct cohesin subunit, RAD21, under basal conditions and following neuronal stimulation with NMDA. Additionally, poisoning of TOP2B with etoposide leads to the formation of DNA single-strand breaks and double-strand breaks (DSBs) [59, 61]. To test whether DSB formation by ETP, and not increased supercoiling, underlies the observed reductions in cohesin occupancy, we also performed RAD21 ChIP-seq in neurons treated with the catalytic TOP2 inhibitor, ICRF-193 (100 μM for 1 h). Annotation of stringent peaks following IDR thresholding revealed that RAD21 preferentially binds gene promoters (Supplementary Fig. S5A), and ontology of genes associated with RAD21 binding sites revealed an enrichment for terms related to neurogenesis and nervous system development (Supplementary Fig. S5B). Intersection of stringent peaks following IDR thresholding revealed that 69.8% (8624/12 359) of SMC1 binding sites overlap with RAD21 binding sites. Similarly, 51.8% of CTCF binding sites (17 533/33 820) were co-occupied by RAD21. Aggregate plots and heatmaps indicated that, like SMC1, RAD21 signals are enriched at CTCF binding sites (Supplementary Fig. S5C), and the CTCF motif was the most significantly enriched motif at RAD21 binding sites (Supplementary Fig. S5D). Overall, RAD21 occupancy patterns recapitulate what is known about cohesin and CTCF binding patterns.

Neuronal stimulation with NMDA markedly reduced RAD21 occupancy across genomic loci, including at 13/15 annotated chromatin states (Supplementary Fig. S6A and B), at the TSS of genes (Supplementary Fig. S6D), and at the boundaries of TADs and loops (Supplementary Fig. S6E and F). Neurons treated with ICRF-193 also displayed a significant reduction in RAD21 occupancy across all 15 chromatin states, the TSS of genes, and the boundaries of TADs and loops (Supplementary Fig. S6A and C–F), mimicking the effects observed with SMC1 in ETP-treated neurons. Together, these results suggest that increased supercoiling following TOP2B inhibition could trigger the disengagement of cohesin in neurons.

Elevated DNA supercoiling disrupts cohesin occupancy on chromatin

We reasoned that if cohesin disengagement in NMDA- and ETP-treated neurons is related to DNA supercoiling, then other paradigms of neuronal stimulation and topoisomerase inhibition should similarly impact cohesin occupancy. To test this idea, we performed subcellular fractionation of neuronal lysates and compared the levels of SMC1 in soluble and chromatin-bound fractions under various conditions. SMC1 could be detected in both soluble and chromatin-bound fractions, and consistent with results from ChIP-seq experiments, neuronal stimulation with NMDA reduced levels of chromatin-bound SMC1 without a significant increase in soluble SMC1 (Fig. 6A, B, E, and F). To determine whether observed reductions in chromatin-bound SMC1 are specific to NMDA, cultured mouse cortical neurons were instead stimulated with bicuculline (BIC; 50 μM for 30 min) to induce activity-dependent transcription [10]. As with NMDA-treated neurons, bicuculline treatments caused a reduction in the levels of chromatin-bound SMC1, suggesting that neuronal stimulation reduces cohesin occupancy on chromatin (Fig. 6A and B).

To next assess how inhibiting topoisomerases affects the association of cohesin with chromatin, fractionation experiments were performed in cultured cortical neurons were treated with either ETP, ICRF-187, or CPT. Consistent with observations in ChIP-seq experiments, ETP-treated neurons showed reduced SMC1 levels in chromatin-bound fractions compared to untreated neurons (Fig. 6C–F). Similar results were observed in cultured cortical neurons treated with the catalytic TOP2 inhibitor, ICRF-187, which, like ICRF-193, also does not induce DSB formation [62], and in neurons treated with the TOP1 inhibitor, CPT (Fig. 6C and D).

We also assessed the nuclear localization of two additional cohesin subunits, SMC3 and RAD21, in response to treatment with NMDA, ETP, or ICRF-187 as described earlier. We observed similar decreases in SMC3 and RAD21 in the chromatin-bound fraction in response to all three treatments (Supplementary Fig. S7A–D). By contrast, a decrease in chromatin-bound CTCF was only observed following NMDA treatment, but not in either ETP- or ICRF-187-treated neurons (Fig. 6G and H) [31]. These results are consistent our previous analysis of CTCF ChIP-seq data in NMDA-treated and ETP-treated neurons and reflects the specific loss of CTCF occupancy from promoters, but not from other genomic regions, under these conditions [31]. The amount of chromatin-bound RNAPII was significantly increased rather than decreased in response to all three treatments (Supplementary Fig. S7E and F). These results are consistent with increased RNAPII engagement following neuronal stimulation and following TOP2B inhibition [46, 63]. These results suggest that the loss of chromatin-bound CTCF and cohesin is specific to these proteins. Furthermore, they indicate that cohesin binding to chromatin can be modulated by the level of supercoiling and that neuronal activity involves the transient disengagement of cohesin from chromatin.

Cohesin disengagement is a conserved feature of stimulus-dependent transcription

Based on our observations in cultured mouse cortical neurons, we sought to determine whether stimulus-dependent transcription in other cell types is also associated with cohesin disengagement. To this end, we utilized publicly available ChIP-seq data to examine changes in the occupancy of the cohesin subunit, RAD21, following LPS treatment of mouse primary B-cells and estradiol (E2) stimulation of human MCF7 cells [64, 65]. Additionally, publicly available RNA-seq data from these cells were used to classify genes as either silent (TPM < 1) or expressed (TPM > 1) within each cell type [66]. RAD21 occupancy was enriched at expressed genes compared to silent genes in mouse primary B-cells (Fig. 7A). Analysis of RAD21 occupancy after bath stimulation with LPS indicated a reduction in both the number of replicated RAD21 peaks (Fig. 7B) and intensity of RAD21 signals at and surrounding the TSS of both expressed and silent genes (Fig. 7C and D).

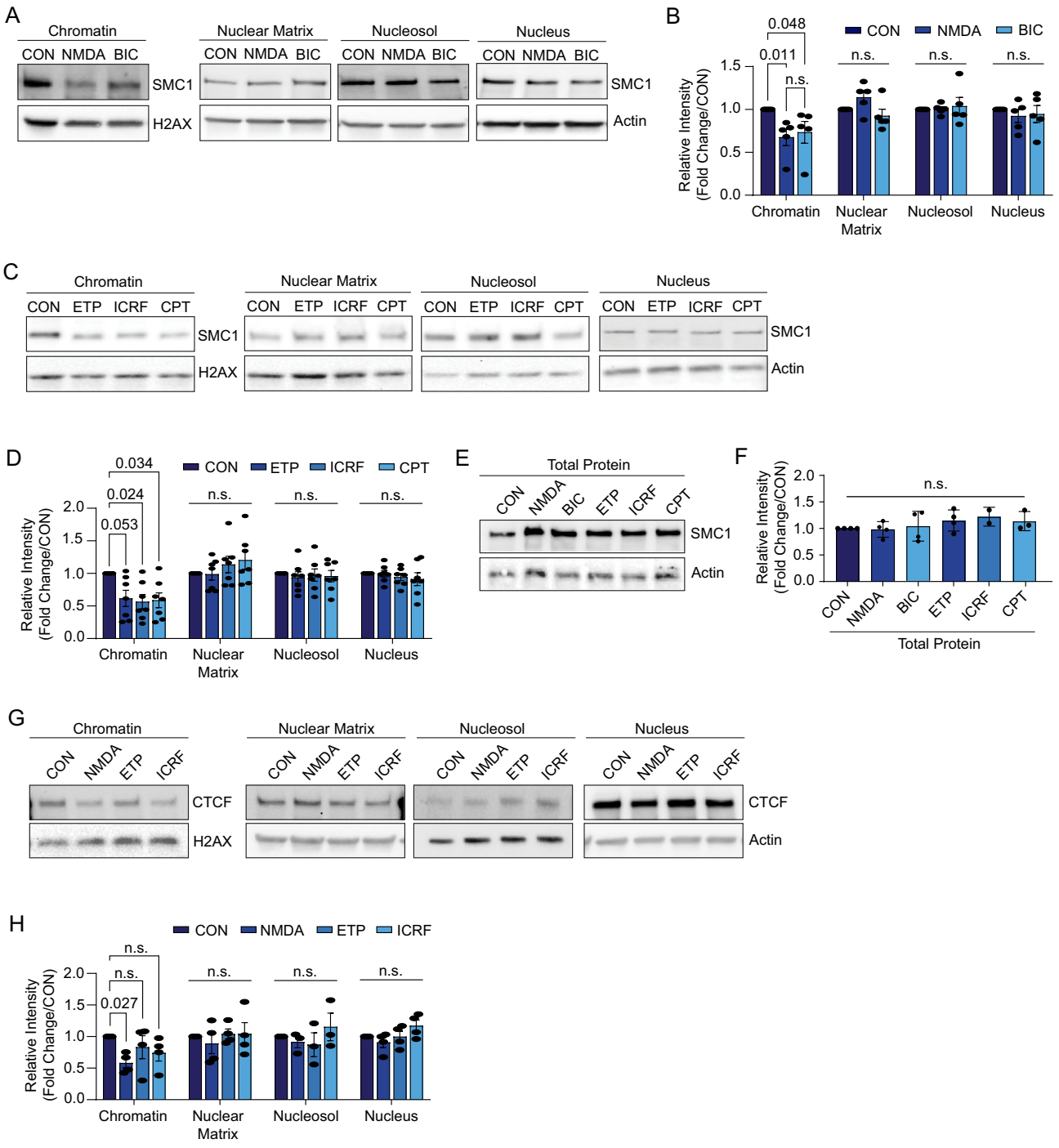

Figure 6. Neuronal activity-dependent loss of SMC1 is related to DNA supercoiling. (**A**, **B**) Lysates from DIV13 mouse cultured cortical neurons were fractionated by differential centrifugation to assess the effect of neuronal stimulation via NMDA (50 μM, 10 min) or bicuculline (BIC; 50 μM, 30–60 min) on the levels of chromatin-bound cohesin. Representative SMC1 western blot images (A) and quantification of SMC1 intensity (B) are shown for the chromatin-bound, nuclear matrix, nucleolus, and nuclear fractions. Actin is shown as a loading control for all fractions except for the chromatin-bound fraction, wherein H2AX was used as a loading control. (**C**, **D**) Lysates from DIV13 mouse cultured cortical neurons were fractionated by differential centrifugation to assess the effect of topoisomerase inhibition via etoposide (ETP; 10 μM, 30 min), ICRF-187 (ICRF; 100 μM, 1 h), or camptothecin (CPT; 10 μM, 1 h) on the levels of chromatin-bound cohesin. Representative SMC1 western blot images (C) and quantification of SMC1 intensity (D) are shown for chromatin-bound, nuclear matrix, nucleolus, and nuclear fractions. Actin is shown as a loading control for all fractions except for the chromatin-bound fraction, wherein H2AX was used as a loading control. Representative SMC1 western blot image (**E**) and quantification of SMC1 intensity (**F**) in the total protein lysate prior to fractionation. (**G**, **H**) Nuclear fractionation of CTCF was assessed in neurons treated with NMDA, ETP, or ICRF as described earlier. Representative CTCF western blot images (G) and quantification of CTCF intensity (H) are shown. Actin is shown as a loading control for all fractions except for the chromatin-bound fraction, wherein H2AX was used as a loading control.

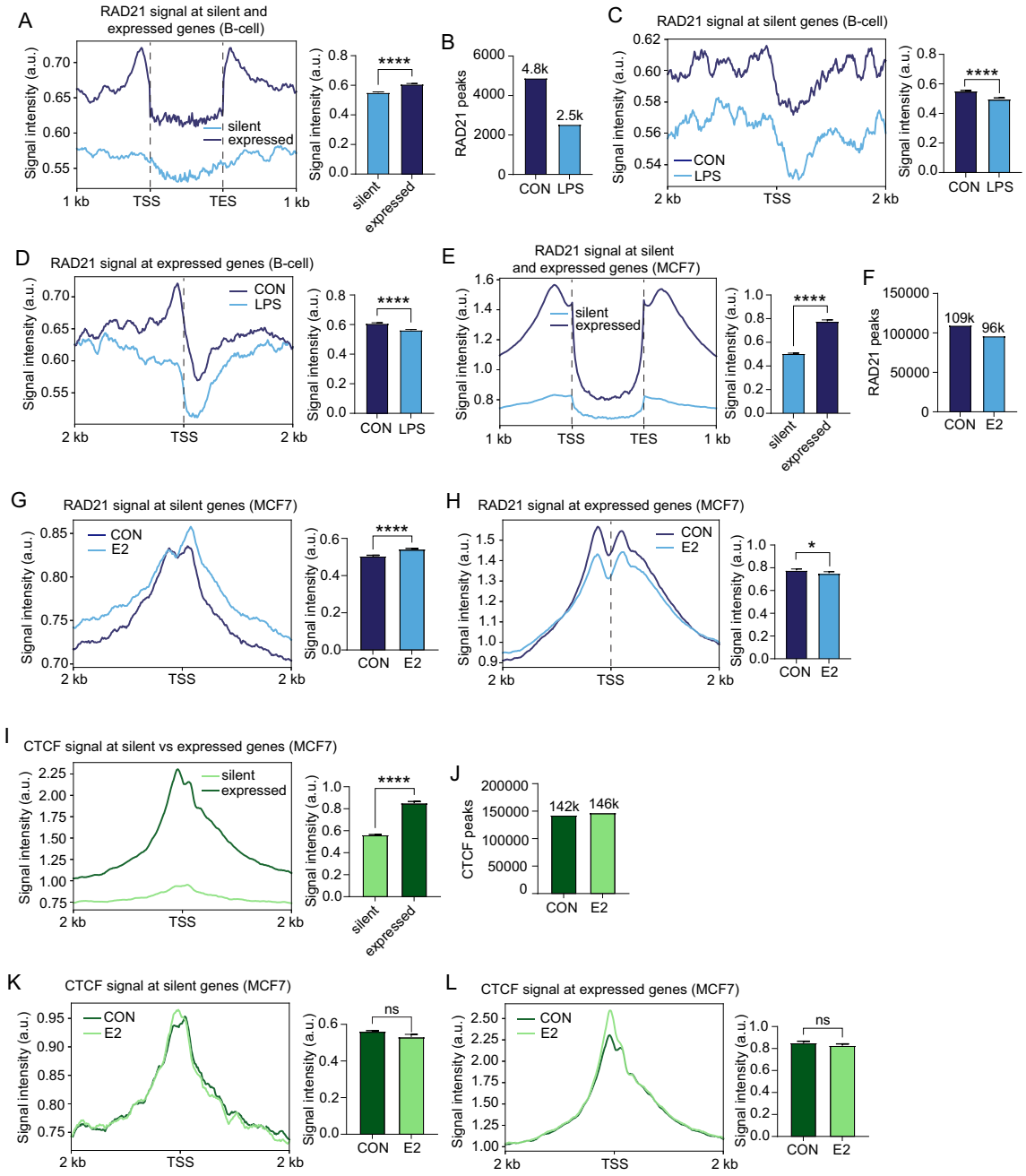

Figure 7. Stimulus-dependent cohesin loss is conserved across multiple cell types and stimulation paradigms. (**A**) Previously published RAD21 ChIP-seq data from untreated primary mouse B cells were used to assess cohesin binding at silent versus expressed genes. Additionally, previously published RNA-seq data from untreated primary mouse B cells was used to define silent (TPM < 1) and expressed (TPM > 1) genes. Aggregate plot of average RAD21 signal (left) and quantification of median signal intensity (right, Mann–Whitney U, $P < .0001$) at silent and expressed genes are shown. (**B**) Number of replicated RAD21 ChIP-seq peaks in untreated and LPS-treated (50 μg/ml, 48 h) primary mouse B cells. (**C**) Aggregate plot of average RAD21 signal (left) and quantification of median RAD21 signal intensity (right, Mann–Whitney U, $P < .0001$) at silent genes in untreated and LPS-treated primary mouse B cells. (**D**) Aggregate plot of average RAD21 signal (left) and quantification of median RAD21 signal intensity (right, Mann–Whitney U, $P < .0001$) at expressed genes in untreated and LPS-treated primary mouse B cells. (**E**) Previously published RNA-seq and RAD21 ChIP-seq data from untreated MCF7 cells were used to assess cohesin binding at silent (TPM < 1) and expressed (TPM > 1) genes. Aggregate plot of average RAD21 signal (left) and quantification of median RAD21 signal intensity (right, Mann–Whitney U, $P < .0001$) at silent and expressed genes are shown. (**F**) Number of replicated RAD21 ChIP-seq peaks in untreated and estradiol-treated (E2, 50 nM, 24 h) MCF7 cells. (**G**) Aggregate plot of average RAD21 signal (left) and quantification of median RAD21 signal intensity (right, Mann–Whitney U, $P < .05$) at expressed genes in untreated and estradiol-treated MCF7 cells. (**H**) Aggregate plot of average RAD21 signal (left) and quantification of median RAD21 signal intensity (right, Mann–Whitney U, $P < .05$) at expressed genes in untreated and estradiol-treated MCF7 cells. (**I**) Previously published RNA-seq and CTCF ChIP-seq data from untreated MCF7 cells were used to assess cohesin binding at silent (TPM < 1) and expressed (TPM > 1) genes. Aggregate plot of average CTCF signal (left) and quantification of median CTCF signal intensity (right, Mann–Whitney U, $P < .0001$) at silent and expressed genes are shown. (**J**) Number of replicated CTCF ChIP-seq peaks in untreated and estradiol-treated (E2, 50 nM, 24 h) MCF7 cells. (**K**) Aggregate plot of average CTCF signal (left) and quantification of median CTCF signal intensity (right, Mann–Whitney U, ns = not significant) at silent genes in untreated and estradiol-treated MCF7 cells. (**L**) Aggregate plot of average CTCF signal (left) and quantification of median CTCF signal intensity (right, Mann–Whitney U, ns = not significant) at expressed genes in untreated and estradiol-treated MCF7 cells.

In human MCF7 cells, RAD21 occupancy was also enriched at expressed genes compared to silent genes (Fig. 7E). The total number of RAD21 peaks genome-wide and RAD21 signals at the TSS of expressed genes were also reduced in MCF7 cells following E2 stimulation; however, such a reduction was not observed at the TSS of silent genes (Fig. 7F–H). In contrast to RAD21, CTCF occupancy in MCF7 was not significantly affected by E2 treatments (Fig. 7I–L), further highlighting the specificity of stimulus-dependent changes in cohesin occupancy. Overall, these results suggest that cohesin disengagement in response to activated transcription can be observed in multiple systems and could be a widely utilized mechanism for establishing activity-dependent chromosome configurations that support transcription.

Discussion

The role of cohesin dynamics in establishing stimulus-dependent chromosome configurations and gene activity patterns is poorly understood. Elaborating these roles in postmitotic neurons is particularly relevant because chromatin reorganization following neuronal activity helps establish gene activity states that underlie learning and other lasting adaptive behaviors [10, 12, 13, 28]. In this regard, our data indicate that cohesin activity relates to that of RNAPII in two major ways. On the one hand, cohesin occupancy at TSSs of actively transcribed genes correlates positively with their level of transcription. These results are consistent with observations in other cells suggesting that either RNAPII or R-loops act as barriers for cohesin-mediated loop extrusion [25, 27, 67–69]. Alternatively, CTCF-RNAPII interactions could explain their correlated levels at the TSS, which could further facilitate cohesin entrapment [70, 71].

On the other hand, neuronal activity-dependent transcription also elevates DNA torsional stress through supercoiling, which disrupts cohesin occupancy genome-wide. Previous studies indicate that transcription is the major source of dynamic supercoiling in cells [52, 55]. Neuronal activity triggers a burst of new transcription of hundreds of genes over a prolonged timescale and increased engagement of RNAPII at thousands of sites genome-wide [63]. This increased transcription is likely to be a major source of increased supercoiling in stimulated neurons. These results are intriguing in the context of single-molecule studies indicating that the efficiency of CTCF to act as a barrier for loop-extruding cohesin increases with increasing tension within the DNA [30]. While tension in these experiments represented the buildup of linear force, a recent preprint suggests that loop-extruding cohesin *in vitro* can also be halted by torque from increased supercoiling [72]. Topoisomerases, particularly topoisomerase II, whose activity was shown to be recruited by cohesin [73], could locally resolve excess supercoiling and facilitate loop extrusion. However, our results suggest that topoisomerases are unable to keep up with supercoiling generated in response to neuronal activity and that the resulting torsion is sufficient to eject cohesin from chromatin. The inability of topoisomerases to immediately and completely resolve dynamic supercoiling is consistent with the widespread detection of dynamic supercoiling upstream of transcriptionally active regions even under basal conditions [52, 74]. Additionally, topoisomerase activity could also be modulated in response to neuronal activity, and this could account for increased supercoiling [59, 60].

Our analysis of additional existing datasets suggests that such cohesin disengagement in response to activated transcription could be a widespread phenomenon. Notably, cohesin occupancy was reported to be largely unaffected in B cells lacking TOP2B in this study, although sites of high TOP2B catalytic engagement in WT cells still showed reductions in RAD21 occupancy in *Top2b*$^{-/-}$ cells [73]. A potential reason for this discrepancy could be that, unlike in postmitotic neurons, B cells also express a second TOP2 isoform, TOP2A, that could potentially compensate for the loss of TOP2B. Precisely how increased DNA torsion results in cohesin ejection from chromatin remains unclear. For instance, increased supercoiling could lead to the unloading of cohesin in a WAPL-dependent manner. Alternatively, increased DNA torsional stress from supercoiling could directly displace cohesin from chromatin independently of WAPL [75]. Analysis of the role of WAPL in stimulus-dependent cohesin occupancy changes could address this issue. Another unanswered question is whether stimulus-dependent disruptions in cohesin occupancy could be functionally relevant for the emergence of stimulus-dependent gene transcription patterns. Hi-C and Micro-C experiments indicate that chromosome contacts in mammalian cells are governed by two distinct mechanisms: loop extrusion by cohesin and compartmentalization of transcriptionally active and inactive regions through phase separation-based mechanisms [76, 77]. Several reports suggest that loop extrusion by cohesin disrupts compartmental chromatin looping interactions and that the loss of cohesin strengthens compartmentalization [18, 24, 78–80]. Based on these results, one possibility is that the supercoiling-dependent loss of cohesin could initially allow for compartment-based scanning and organization of chromosomes. Such compartment-based scanning could explain how many stimulus-induced genes, including neuronal immediate early genes, establish enhancer-promoter contacts independently of cohesin [28, 81, 82]. The eventual resolution of supercoiling by topoisomerases would then allow for the re-engagement of cohesin. We propose that the reactivation of loop extrusion in this manner could not only refine compartment-based interactions but also facilitate long-range enhancer-promoter contacts that in neurons were shown to regulate the transcription of secondary response genes [28]. Patterns of changes in chromosomal contacts in hippocampal neurons following KA stimulation are consistent with such a model. While changes in topoisomerase activity and supercoiling have been shown to affect transcription initiation and the movement of RNAPII [46, 55], our findings here demonstrate how torsion from DNA supercoiling could impact transcription by additionally promoting the formation of stimulus-driven chromatin topologies [83].

Acknowledgements

Author contributions: Study design - M.C. and R.M.; Investigation - All authors; Methology - All authors; Writing, Review, and Editing - All authors.

Supplementary data

Supplementary data is available at NAR online.

Conflict of interest

None declared.

Funding

This work was supported by the National Institute of Mental Health [grant numbers MH120132, MH135952, MH130399 to R.M.; and grant number MH134200 to I.D.R.] and the Cancer Prevention Research Institute of Texas [grant number RP210041 to M.C.]. Funding to pay the Open Access publication charges for this article was provided by NIMH grant no. MH135952.

Data availability

ChIP-seq datasets from ENCODE or the GEO repository were used throughout the manuscript, and a complete list is available in Supplementary Table S2. Data generated for this manuscript are publicly available under accessions GSE282195 and GSE282196.

References

1. Luger K, Mader AW, Richmond RK *et al.* Crystal structure of the nucleosome core particle at 2.8 A resolution. *Nature* 1997;389:251–60. https://doi.org/10.1038/38444
2. Lieberman-Aiden E, van Berkum NL, Williams L *et al.* Comprehensive mapping of long-range interactions reveals folding principles of the human genome. *Science* 2009;326:289–93. https://doi.org/10.1126/science.1181369
3. da Costa-Nunes JA, Noordermeer D. TADs: dynamic structures to create stable regulatory functions. *Curr Opin Struct Biol* 2023;81:102622. https://doi.org/10.1016/j.sbi.2023.102622
4. Oji A, Choubani L, Miura H *et al.* Structure and dynamics of nuclear A/B compartments and subcompartments. *Curr Opin Cell Biol* 2024;90:102406. https://doi.org/10.1016/j.ceb.2024.102406
5. Winick-Ng W, Kukalev A, Harabula I *et al.* Cell-type specialization is encoded by specific chromatin topologies. *Nature* 2021;599:684–91. https://doi.org/10.1038/s41586-021-04081-2
6. Flavahan WA, Drier Y, Liau BB *et al.* Insulator dysfunction and oncogene activation in IDH mutant gliomas. *Nature* 2016;529:110–4. https://doi.org/10.1038/nature16490
7. Franke M, Ibrahim DM, Andrey G *et al.* Formation of new chromatin domains determines pathogenicity of genomic duplications. *Nature* 2016;538:265–9. https://doi.org/10.1038/nature19800
8. Hnisz D, Weintraub AS, Day DS *et al.* Activation of proto-oncogenes by disruption of chromosome neighborhoods. *Science* 2016;351:1454–8. https://doi.org/10.1126/science.aad9024
9. Rajarajan P, Borrman T, Liao W *et al.* Neuron-specific signatures in the chromosomal connectome associated with schizophrenia risk. *Science* 2018;362:eaat4311. https://doi.org/10.1126/science.aat4311 362.
10. Beagan JA, Pastuzyn ED, Fernandez LR *et al.* Three-dimensional genome restructuring across timescales of activity-induced neuronal gene expression. *Nat Neurosci* 2020;23:707–17. https://doi.org/10.1038/s41593-020-0634-6
11. Su Y, Shin J, Zhong C *et al.* Neuronal activity modifies the chromatin accessibility landscape in the adult brain. *Nat Neurosci* 2017;20:476–83. https://doi.org/10.1038/nn.4494
12. Yap EL, Greenberg ME. Activity-regulated transcription: bridging the gap between neural activity and behavior. *Neuron* 2018;100:330–48. https://doi.org/10.1016/j.neuron.2018.10.013
13. Madabhushi R, Kim TK. Emerging themes in neuronal activity-dependent gene expression. *Mol Cell Neurosci* 2018;87:27–34. https://doi.org/10.1016/j.mcn.2017.11.009
14. Davidson IF, Peters JM. Genome folding through loop extrusion by SMC complexes. *Nat Rev Mol Cell Biol* 2021;22:445–64. https://doi.org/10.1038/s41580-021-00349-7
15. Rittenhouse NL, Dowen JM. Cohesin regulation and roles in chromosome structure and function. *Curr Opin Genet Dev* 2024;85:102159. https://doi.org/10.1016/j.gde.2024.102159
16. Wendt KS, Yoshida K, Itoh T *et al.* Cohesin mediates transcriptional insulation by CCCTC-binding factor. *Nature* 2008;451:796–801. https://doi.org/10.1038/nature06634
17. Parelho V, Hadjur S, Spivakov M *et al.* Cohesins functionally associate with CTCF on mammalian chromosome arms. *Cell* 2008;132:422–33. https://doi.org/10.1016/j.cell.2008.01.011
18. Rao SSP, Huang SC, Glenn St Hilaire B *et al.* Cohesin loss eliminates all loop domains. *Cell* 2017;171:305–20. https://doi.org/10.1016/j.cell.2017.09.026
19. Fudenberg G, Imakaev M, Lu C *et al.* Formation of chromosomal domains by loop extrusion. *Cell Rep* 2016;15:2038–49. https://doi.org/10.1016/j.celrep.2016.04.085
20. Sanborn AL, Rao SS, Huang SC *et al.* Chromatin extrusion explains key features of loop and domain formation in wild-type and engineered genomes. *Proc Natl Acad Sci USA* 2015;112:E6456–65. https://doi.org/10.1073/pnas.1518552112
21. Davidson IF, Bauer B, Goetz D *et al.* DNA loop extrusion by human cohesin. *Science* 2019;366:1338–45. https://doi.org/10.1126/science.aaz3418
22. Kim Y, Shi Z, Zhang H *et al.* Human cohesin compacts DNA by loop extrusion. *Science* 2019;366:1345–9. https://doi.org/10.1126/science.aaz4475
23. Bauer BW, Davidson IF, Canena D *et al.* Cohesin mediates DNA loop extrusion by a "swing and clamp" mechanism. *Cell* 2021;184:5448–64. https://doi.org/10.1016/j.cell.2021.09.016
24. Wutz G, Varnai C, Nagasaka K *et al.* Topologically associating domains and chromatin loops depend on cohesin and are regulated by CTCF, WAPL, and PDS5 proteins. *EMBO J* 2017;36:3573–99. https://doi.org/10.15252/embj.201798004
25. Zhang S, Ubelmesser N, Barbieri M *et al.* Enhancer-promoter contact formation requires RNAPII and antagonizes loop extrusion. *Nat Genet* 2023;55:832–40. https://doi.org/10.1038/s41588-023-01364-4
26. Barshad G, Lewis JJ, Chivu AG *et al.* RNA polymerase II dynamics shape enhancer-promoter interactions. *Nat Genet* 2023;55:1370–80. https://doi.org/10.1038/s41588-023-01442-7
27. Zhang H, Shi Z, Banigan EJ *et al.* CTCF and R-loops are boundaries of cohesin-mediated DNA looping. *Mol Cell* 2023;83:2856–71. https://doi.org/10.1016/j.molcel.2023.07.006
28. Calderon L, Weiss FD, Beagan JA *et al.* Cohesin-dependence of neuronal gene expression relates to chromatin loop length. *eLife* 2022;11:e76539. https://doi.org/10.7554/eLife.76539
29. Grabowska A, Sas-Nowosielska H, Wojtas B *et al.* Activation-induced chromatin reorganization in neurons depends on HDAC1 activity. *Cell Rep* 2022;38:110352. https://doi.org/10.1016/j.celrep.2022.110352
30. Davidson IF, Barth R, Zaczek M *et al.* CTCF is a DNA-tension-dependent barrier to cohesin-mediated loop extrusion. *Nature* 2023;616:822–7. https://doi.org/10.1038/s41586-023-05961-5
31. Crewe M, Segev A, Rueda R *et al.* Atypical modes of CTCF binding facilitate tissue-specific and neuronal activity-dependent gene expression states. *Mol Neurobiol* 2024;61:3240–57. https://doi.org/10.1007/s12035-023-03762-5
32. Landt SG, Marinov GK, Kundaje A *et al.* ChIP-seq guidelines and practices of the ENCODE and modENCODE consortia. *Genome Res* 2012;22:1813–31. https://doi.org/10.1101/gr.136184.111
33. Zhang Y, Liu T, Meyer CA *et al.* Model-based analysis of ChIP-Seq (MACS). *Genome Biol* 2008;9:1–9. https://doi.org/10.1186/gb-2008-9-9-r137
34. Kuhn RM, Haussler D, Kent WJ. The UCSC genome browser and associated tools. *Brief Bioinform* 2013;14:144–61. https://doi.org/10.1093/bib/bbs038
35. Kim D, Pertea G, Trapnell C *et al.* TopHat2: accurate alignment of transcriptomes in the presence of insertions, deletions and gene fusions. *Genome Biol* 2013;14:R36. https://doi.org/10.1186/gb-2013-14-4-r36

36. Putri GH, Anders S, Pyl PT *et al.* Analysing high-throughput sequencing data in Python with HTSeq 2.0. *Bioinformatics* 2022;38:2943–5. https://doi.org/10.1093/bioinformatics/btac166
37. Love MI, Huber W, Anders S. Moderated estimation of fold change and dispersion for RNA-seq data with DESeq2. *Genome Biol* 2014;15:550. https://doi.org/10.1186/s13059-014-0550-8
38. Ernst J, Kellis M. Chromatin-state discovery and genome annotation with ChromHMM. *Nat Protoc* 2017;12:2478–92. https://doi.org/10.1038/nprot.2017.124
39. Yu G, Wang LG, He QY. ChIPseeker: an R/Bioconductor package for ChIP peak annotation, comparison and visualization. *Bioinformatics* 2015;31:2382–3. https://doi.org/10.1093/bioinformatics/btv145
40. Wu T, Hu E, Xu S *et al.* clusterProfiler 4.0: a universal enrichment tool for interpreting omics data. *Innovation (Camb)* 2021;2:100141.
41. Bonev B, Mendelson Cohen N, Szabo Q *et al.* Multiscale 3D genome rewiring during mouse neural development. *Cell* 2017;171:557–72. https://doi.org/10.1016/j.cell.2017.09.043
42. Fernandez-Albert J, Lipinski M, Lopez-Cascales MT *et al.* Immediate and deferred epigenomic signatures of *in vivo* neuronal activation in mouse hippocampus. *Nat Neurosci* 2019;22:1718–30. https://doi.org/10.1038/s41593-019-0476-2
43. Durand NC, Shamim MS, Machol I *et al.* Juicer provides a one-click system for analyzing loop-resolution Hi-C experiments. *Cell Syst* 2016;3:95–8. https://doi.org/10.1016/j.cels.2016.07.002
44. Durand NC, Robinson JT, Shamim MS *et al.* Juicebox provides a visualization system for Hi-C contact maps with unlimited zoom. *Cell Syst* 2016;3:99–101. https://doi.org/10.1016/j.cels.2015.07.012
45. Ramírez F, Dündar F, Diehl S *et al.* deepTools: a flexible platform for exploring deep-sequencing data. *Nucleic Acids Res* 2014;42:W187–91.
46. Segev A, Heady L, Crewe M *et al.* Mapping catalytically engaged TOP2B in neurons reveals the principles of topoisomerase action within the genome. *Cell Rep* 2024;43:113809. https://doi.org/10.1016/j.celrep.2024.113809
47. Barbieri E, Hill C, Quesnel-Vallieres M *et al.* Rapid and scalable profiling of nascent RNA with fastGRO. *Cell Rep* 2020;33:108373. https://doi.org/10.1016/j.celrep.2020.108373
48. Wang D, Garcia-Bassets I, Benner C *et al.* Reprogramming transcription by distinct classes of enhancers functionally defined by eRNA. *Nature* 2011;474:390–4. https://doi.org/10.1038/nature10006
49. Gorkin DU, Barozzi I, Zhao Y *et al.* An atlas of dynamic chromatin landscapes in mouse fetal development. *Nature* 2020;583:744–51. https://doi.org/10.1038/s41586-020-2093-3
50. Consortium EP, Moore JE, Purcaro MJ *et al.* Expanded encyclopaedias of DNA elements in the human and mouse genomes. *Nature* 2020;583:699–710. https://doi.org/10.1038/s41586-020-2493-4
51. Achar YJ, Adhil M, Choudhary R *et al.* Negative supercoil at gene boundaries modulates gene topology. *Nature* 2020;577:701–5. https://doi.org/10.1038/s41586-020-1934-4
52. Kouzine F, Gupta A, Baranello L *et al.* Transcription-dependent dynamic supercoiling is a short-range genomic force. *Nat Struct Mol Biol* 2013;20:396–403. https://doi.org/10.1038/nsmb.2517
53. Liu LF, Wang JC. Supercoiling of the DNA template during transcription. *Proc Natl Acad Sci USA* 1987;84:7024–7. https://doi.org/10.1073/pnas.84.20.7024
54. Naughton C, Avlonitis N, Corless S *et al.* Transcription forms and remodels supercoiling domains unfolding large-scale chromatin structures. *Nat Struct Mol Biol* 2013;20:387–95. https://doi.org/10.1038/nsmb.2509
55. Teves SS, Henikoff S. Transcription-generated torsional stress destabilizes nucleosomes. *Nat Struct Mol Biol* 2014;21:88–94. https://doi.org/10.1038/nsmb.2723
56. Yao Q, Zhu L, Shi Z *et al.* Topoisomerase-modulated genome-wide DNA supercoiling domains colocalize with nuclear compartments and regulate human gene expression. *Nat Struct Mol Biol* 2025;32:48–61. https://doi.org/10.1038/s41594-024-01377-5
57. Bermudez I, Garcia-Martinez J, Perez-Ortin JE *et al.* A method for genome-wide analysis of DNA helical tension by means of psoralen-DNA photobinding. *Nucleic Acids Res* 2010;38:e182. https://doi.org/10.1093/nar/gkq687
58. Madabhushi R. The roles of DNA topoisomerase IIbeta in transcription. *Int J Mol Sci* 2018;19:1917. https://doi.org/10.3390/ijms19071917
59. Madabhushi R, Gao F, Pfenning AR *et al.* Activity-induced DNA breaks govern the expression of neuronal early-response genes. *Cell* 2015;161:1592–605. https://doi.org/10.1016/j.cell.2015.05.032
60. Delint-Ramirez I, Konada L, Heady L *et al.* Calcineurin dephosphorylates topoisomerase IIbeta and regulates the formation of neuronal-activity-induced DNA breaks. *Mol Cell* 2022;82:3794–809. https://doi.org/10.1016/j.molcel.2022.09.012
61. Dobbin MM, Madabhushi R, Pan L *et al.* SIRT1 collaborates with ATM and HDAC1 to maintain genomic stability in neurons. *Nat Neurosci* 2013;16:1008–15. https://doi.org/10.1038/nn.3460
62. Hasinoff BB, Kuschak TI, Yalowich JC *et al.* A QSAR study comparing the cytotoxicity and DNA topoisomerase II inhibitory effects of bisdioxopiperazine analogs of ICRF-187 (dexrazoxane). *Biochem Pharmacol* 1995;50:953–8. https://doi.org/10.1016/0006-2952(95)00218-O
63. Kim TK, Hemberg M, Gray JM *et al.* Widespread transcription at neuronal activity-regulated enhancers. *Nature* 2010;465:182–7. https://doi.org/10.1038/nature09033
64. Gunal-Sadik G, Paszkowski-Rogacz M, Singaravelu K *et al.* Stage-specific binding profiles of cohesin in resting and activated B lymphocytes suggest a role for cohesin in immunoglobulin class switching and maturation. *PLoS One* 2014;9:e111748. https://doi.org/10.1371/journal.pone.0111748
65. Wang J, Bando M, Shirahige K *et al.* Large-scale multi-omics analysis suggests specific roles for intragenic cohesin in transcriptional regulation. *Nat Commun* 2022;13:3218. https://doi.org/10.1038/s41467-022-30792-9
66. Gao H, Zhao Y, Zhao S *et al.* The ICF2 gene Zbtb24 specifically regulates the differentiation of B1 cells via promoting heme synthesis. *Cell Mol Biol Lett* 2024;29:123. https://doi.org/10.1186/s11658-024-00641-2
67. Kagey MH, Newman JJ, Bilodeau S *et al.* Mediator and cohesin connect gene expression and chromatin architecture. *Nature* 2010;467:430–5. https://doi.org/10.1038/nature09380
68. Zuin J, Franke V, van Ijcken WF *et al.* A cohesin-independent role for NIPBL at promoters provides insights in CdLS. *PLoS Genet* 2014;10:e1004153. https://doi.org/10.1371/journal.pgen.1004153
69. Busslinger GA, Stocsits RR, van der Lelij P *et al.* Cohesin is positioned in mammalian genomes by transcription, CTCF and Wapl. *Nature* 2017;544:503–7. https://doi.org/10.1038/nature22063
70. Chernukhin I, Shamsuddin S, Kang SY *et al.* CTCF interacts with and recruits the largest subunit of RNA polymerase II to CTCF target sites genome-wide. *Mol Cell Biol* 2007;27:1631–48. https://doi.org/10.1128/MCB.01993-06
71. Lee BK, Bhinge AA, Battenhouse A *et al.* Cell-type specific and combinatorial usage of diverse transcription factors revealed by genome-wide binding studies in multiple human cells. *Genome Res* 2012;22:9–24. https://doi.org/10.1101/gr.127597.111
72. Davidson IF, Barth R, Horn S *et al.* Cohesin supercoils DNA during loop extrusion. *Cell Rep* 2025;44:115856. https://doi.org/10.1101/2024.03.22.586228
73. Canela A, Maman Y, Huang SN *et al.* Topoisomerase II-induced chromosome breakage and translocation is determined by chromosome architecture and transcriptional activity. *Mol Cell* 2019;75:252–66. https://doi.org/10.1016/j.molcel.2019.04.030
74. Kouzine F, Sanford S, Elisha-Feil Z *et al.* The functional response of upstream DNA to dynamic supercoiling in vivo. *Nat Struct Mol Biol* 2008;15:146–54. https://doi.org/10.1038/nsmb.1372

75. Neguembor MV, Martin L, Castells-Garcia A *et al.* Transcription-mediated supercoiling regulates genome folding and loop formation. *Mol Cell* 2021;81:3065–81. https://doi.org/10.1016/j.molcel.2021.06.009
76. Mirny LA, Imakaev M, Abdennur N. Two major mechanisms of chromosome organization. *Curr Opin Cell Biol* 2019;58:142–52. https://doi.org/10.1016/j.ceb.2019.05.001
77. Magnitov M, de Wit E. Attraction and disruption: how loop extrusion and compartmentalisation shape the nuclear genome. *Curr Opin Genet Dev* 2024;86:102194. https://doi.org/10.1016/j.gde.2024.102194
78. Schwarzer W, Abdennur N, Goloborodko A *et al.* Two independent modes of chromatin organization revealed by cohesin removal. *Nature* 2017;551:51–6. https://doi.org/10.1038/nature24281
79. Gassler J, Brandao HB, Imakaev M *et al.* A mechanism of cohesin-dependent loop extrusion organizes zygotic genome architecture. *EMBO J* 2017;36:3600–18. https://doi.org/10.15252/embj.201798083
80. Rhodes JDP, Feldmann A, Hernandez-Rodriguez B *et al.* Cohesin disrupts Polycomb-dependent chromosome interactions in embryonic stem cells. *Cell Rep* 2020;30:820–35. https://doi.org/10.1016/j.celrep.2019.12.057e810.
81. Hsieh TS, Cattoglio C, Slobodyanyuk E *et al.* Resolving the 3D landscape of transcription-linked mammalian chromatin folding. *Mol Cell* 2020;78:539–53. https://doi.org/10.1016/j.molcel.2020.03.002
82. Hsieh TS, Cattoglio C, Slobodyanyuk E *et al.* Enhancer-promoter interactions and transcription are largely maintained upon acute loss of CTCF, cohesin, WAPL or YY1. *Nat Genet* 2022;54:1919–32. https://doi.org/10.1038/s41588-022-01223-8
83. Hehmeyer J, Spitz F, Marlow H. Shifting landscapes: the role of 3D genomic organizations in gene regulatory strategies. *Curr Opin Genet Dev* 2023;81:102064. https://doi.org/10.1016/j.gde.2023.102064

Received: December 8, 2024. **Revised:** May 5, 2026. **Accepted:** May 17, 2026